

Cluster Rearrangement by Chiral Charge Order in Lacunar Spinel GaNb_4Se_8

Shunsuke Kitou,^{1,*} Masaki Gen,² Yuiga Nakamura,³ Yusuke Tokunaga,¹ Taka-hisa Arima^{1,2}

¹*Department of Advanced Materials Science, The University of Tokyo, Kashiwa 277-8561, Japan.*

²*RIKEN Center for Emergent Matter Science, Wako 351-0198, Japan.*

³*Japan Synchrotron Radiation Research Institute (JASRI), SPring-8; Hyogo 679-5198, Japan.*

ABSTRACT: Transition-metal atoms with d electrons sometimes form clusters in crystals, which significantly affect the physical properties. Such a cluster formation frequently accompanies a change in the crystal system, leading to the presence of domains with different crystal orientations. In particular, the cubic symmetry is rarely retained after the cluster formation. Here, we identify a cubic-to-cubic phase transition in lacunar spinel GaNb_4Se_8 , where the change in the lattice parameter is less than 0.0001%. Each $\text{Nb}^{3.25+}$ tetramer with seven $4d$ electrons is distorted into an Nb^{3+} trimer and an Nb^{4+} monomer induced by charge disproportionation among Nb ions. While the Nb^{3+} trimer with six $4d$ electrons forms spin-singlets in the σ -bonding orbitals for three Nb-Nb bonds, a localized

$S = 1/2$ spin remains on the Nb^{4+} ion. Furthermore, a local electric dipole moment is induced along the 3-fold rotation axis of each distorted tetramer by the cluster rearrangement. The electric dipole moments are regularly arranged to maintain cubic symmetry, giving rise to chiral order.

INTRODUCTION

Transport and magnetic properties in transition-metal chalcogenides are dominated by the orbital state of transition metals surrounded by the chalcogen elements of O, S, and Se. Early transition-metal atoms sometimes form clusters,^{1,2} lowering the energy by sharing bonding d electrons. For instance, rutile-type vanadium dioxide VO_2 with a tetragonal lattice undergoes a metal-insulator transition due to V-V dimerization,³⁻⁷ leading to monoclinic distortion of the entire lattice. Such significant changes in physical properties due to cluster formations may be phase-controlled by external fields, allowing for applications in materials such as memory^{8,9} and sensors.^{10,11} However, cluster formations frequently induce substantial local distortion, causing pronounced anisotropic deformation of the overall lattice and the emergence of domains with varying crystal orientations. In particular, the cubic symmetry is rarely retained after the cluster formation. The significant distortion becomes the primary rate-limiting factor for phase switching. Therefore, the search for materials that form clusters without a reduction in lattice symmetry and with minimal lattice distortion is crucial not only for fundamental research but also for the development of practical materials.

β -Pyrochlore oxide CsW_2O_6 is a rare material that preserves cubic lattice symmetry across the phase transition accompanied by cluster formations. CsW_2O_6 with a half-integer average valence of $\text{W}^{5.5+}$ ($5d^{0.5}$) undergoes a metal-insulator transition at 215 K,^{12,13} where the space group changes from $Fd\bar{3}m$ to $P2_13$. The pyrochlore network of $\text{W}^{5.5+}$ in the higher-temperature cubic phase is distorted three-dimensionally to form regular $\text{W}^{5.33+}$ ($5d^{2/3}$) trimers and isolated W^{6+} ($5d^0$) ions in the lower-temperature cubic phase, where the lattice constant increases by $\sim 0.004\%$ with the cubic-to-cubic phase transition. The $\text{W}^{5.33+}$ trimer has two $5d$ electrons, indicating a three-centered-two-electron bond formation.¹³ Such a cluster formation leads to the nonmagnetic insulating nature in the lower-temperature cubic phase. In this system, the cubic symmetry is maintained by orienting adjacent W trimers not parallel to each other.

Lacunar spinel compounds GaM_4X_8 ($M = \text{V}, \text{Nb}, \text{Mo}, \text{Ta}$, and $X = \text{S}, \text{Se}$) are Mott insulator systems that exhibit various electronic and magnetic properties, such as pressure-induced superconductivity,¹⁴⁻¹⁷ negative colossal magnetoresistance,¹⁸ spin-singlet state,^{19,20} spin-orbit entangled molecular J_{eff} state,²⁰⁻²⁵ and magnetic skyrmions.²⁶⁻²⁹ Since the formal valence of M is $3.25+$, the average number of d electrons are $7/4$ and $11/4$ for group V ($M = \text{V}, \text{Nb}, \text{Ta}$) and group VI ($M = \text{Mo}$) transition metals, respectively. Since only half of the tetrahedral sites are occupied by Ga atoms, the pyrochlore network of M atoms takes on a breathing-type structure, resulting in M_4 tetrahedral clusters. The space group is noncentrosymmetric $F\bar{4}3m$. As cooling GaM_4X_8 with $M = \text{V}$ and Mo, the overall lattice is distorted along one of the cubic $\langle 111 \rangle$ axes, resulting in the rhombohedral polar $R\bar{3}m$ space group.^{30,31} This rhombohedral distortion is understood as a cooperative Jahn-Teller distortion of the M_4 molecular orbitals. Furthermore, in a

magnetic field, magnetic orders including a skyrmion lattice emerge at lower temperatures in the rhombohedral phase.²⁶⁻²⁹ In contrast, GaM_4X_8 with $M = \text{Nb}$ and Ta exhibit different types of distortion. The lattice of GaTa_4Se_8 changes to tetragonal below $T_M = 50 \text{ K}$.^{20,25} GaNb_4S_8 and GaNb_4Se_8 have orthorhombic distortion in the low-temperature phase below $T_M = 32$ and 33 K , respectively.^{20,32} These low-temperature phases are characterized by nonmagnetic (spin-singlet) nature confirmed by nuclear magnetic resonance.^{19,20} However, GaNb_4Se_8 undergoes another phase transition at $T_C = 50 \text{ K}$.²⁰ Powder X-ray diffraction (XRD) experiments suggest the cubic space group $P2_13$ in the intermediate-temperature phase between T_M and T_C .²⁰

In this study, we perform single-crystal synchrotron XRD experiments to reveal the crystal structure in the intermediate-temperature phase of GaNb_4Se_8 . Nb clusters are found to be rearranged to form a chiral charge order associated with charge disproportionation among Nb ions. The cubic-to-cubic phase transition maintains the overall lattice and total magnetic moment with an exquisite cluster rearrangement, which is different from the first-order phase transition to a nonmagnetic state in CsW_2O_6 .¹³

EXPERIMENTS

Polycrystalline samples of GaNb_4Se_8 were synthesized by a solid-state reaction of high-purity ingredients Ga (99.99%), Nb (99.9%), and Se (99.999%). The stoichiometric powder, weighing 2 g, was sealed in an evacuated quartz ampule and heated at $900 \text{ }^\circ\text{C}$ for 70 h. 0.5 g of the obtained polycrystalline material was used as a source for single-crystal growth by chemical vapor transport. The growth was performed using PtCl_2 as a transport agent in a quartz ampule at temperatures between 900 and $950 \text{ }^\circ\text{C}$ for 240 h.

Magnetization measurements were performed by a superconducting quantum interference device (MPMS, Quantum Design) between 2 and 300 K in magnetic fields of up to 7 T. Heat capacity was measured by the thermal relaxation method by using a commercial system (Quantum Design: PPMS). Thermal expansion $\Delta L/L$ along the [111] axis was measured by the fiber-Bragg-grating (FBG) technique using an optical sensing instrument (Hyperion si155, LUNA) in a cryostat equipped with a superconducting magnet (Oxford Spectromag). Although the FBG method causes quantitative errors due to incomplete coupling between the fiber and the sample,³³ one can detect the sample strain with an accuracy of $\Delta L/L \sim 0.0001\%$. XRD experiments were performed using a single crystal of $52 \times 48 \times 35 \mu\text{m}^3$ on BL02B1 at a synchrotron facility SPring-8 in Japan.³⁴ A He-gas-blowing device was employed for controlling the temperature between 34 and 300 K. The X-ray wavelength was $\lambda = 0.30956 \text{ \AA}$. A two-dimensional detector CdTe PILATUS was used to record the diffraction pattern. The intensities of Bragg reflections with the interplane distance $d > 0.28 \text{ \AA}$ were collected by CrysAlisPro program.³⁵ Intensities of equivalent reflections were averaged and the structural parameters were refined by using Jana2006.³⁶ Crystal structures are visualized by using VESTA.³⁷

RESULTS AND DISCUSSION

Figures 1a and 1b show the crystal structure of GaNb_4Se_8 at 70 K in the high-temperature phase. Merohedral domains corresponding to space inversion were not observed. The deficiency of the Ga site is found to be less than 1%. Nb atoms form regular tetrahedra. The intra- and inter-clusters distances between Nb atoms are 3.0345(4) and 4.3295(5) Å , respectively. Details of the structural parameters are summarized in Tables S1 and S2. Figure 1c shows the molecular orbital scheme of a Nb_4 cluster. The t_{2g} atomic

orbitals of a Nb ion in a regular Se_6 octahedron split into five types of molecular orbitals with different energies under T_d symmetry due to the Nb_4 cluster formation.³⁸ The t_2 molecular orbitals accommodate one electron, resulting in an $S = 1/2$ state when ignoring the spin-orbit interaction.

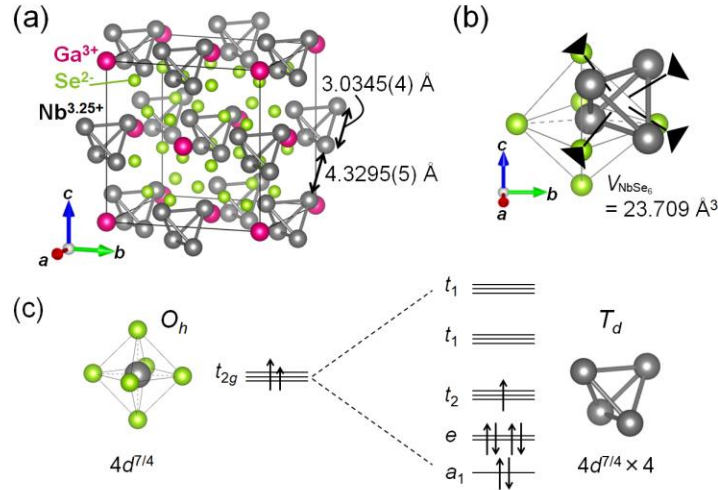


Figure 1. (a) Crystal structure of GaNb_4Se_8 at 70 K in the high-temperature phase. (b) Nb_4 tetrahedron (gray) and Se_6 octahedron (green) in GaNb_4Se_8 . Solid triangles indicate 3-fold rotation axes along $\langle 111 \rangle$. (c) Schematic of the molecular orbital formation of the Nb tetramer. The t_{2g} atomic orbitals under O_h symmetry at the four Nb sites form five molecular orbitals with different energies under T_d symmetry.

Figure 2a shows the temperature dependence of magnetic susceptibility χ for $H \parallel [111]$ of GaNb_4Se_8 . There is no anisotropy in the magnetic susceptibility when the external magnetic fields are applied in the $[111]$, $[110]$, and $[001]$ directions (Figure S1 and Table S5). We perform a Curie-Weiss fit for the magnetic susceptibility curve using a formula

$\chi(T) = \chi_0 + C/(T - \Theta)$, where χ_0 , C , and Θ are temperature independent components of χ , Curie constant, and Weiss temperature, respectively. The fit above 150 K yields $\chi_0 = -6.2 \times 10^{-5}$ emu/mol, $C = 0.3033$ K emu/mol, and $\Theta = -142.6$ K. The Curie constant gives the effective magnetic moment $\mu_{\text{eff}} = 1.558\mu_{\text{B}}/\text{f.u.}$, which is slightly smaller than the expected value of $1.73\mu_{\text{B}}/\text{f.u.}$ for $S = 1/2$. A kink and a sharp decrease are observed in χ at $T_{\text{C}} = 50$ K and $T_{\text{M}} = 31$ K, respectively. These results are consistent with previous reports.^{20,39} A thermal hysteresis indicates the first-order nature of the phase transition around T_{M} , as shown in the inset of Figure 2a. Furthermore, T_{M} slightly decreases with increasing external magnetic field (Figure S2).

Figure 2b shows the temperature dependence of heat capacity divided by temperature (C_p/T) at 0 T. Broad and sharp peaks are observed at T_{C} and T_{M} , which indicate second- and first-order like phase transitions, respectively. The low-temperature behavior deviates from the Debye model ($C_p \propto T^3$) (Figure S3a). The $C_p \propto T^2$ component appears at low temperatures, which is not a typical behavior of a three-dimensional antiferromagnet, where the magnon contribution C_p^{mag} is proportional to T^3 . The entropy change $\Delta S_{\text{C}} = 1.0$ J/(mol K) associated with the second-order like phase transition at T_{C} is estimated from C_p in $40 \text{ K} \leq T \leq 50 \text{ K}$. Since the heat capacity was measured by the thermal relaxation method, the released entropy in the first-order phase transition at T_{M} could not be accurately estimated from C_p . The entropy change at T_{M} is estimated from the temperature dependence and the external magnetic field dependence of the magnetic susceptibilities as $\Delta S_{\text{M}} = 6.8$ J/(mol K) (Figure S2). In the heat capacity measurements, T_{M} decreases with increasing the external magnetic field (Figure S3c), which is consistent

with our magnetic susceptibility results and the previous report.³⁹ In contrast, T_C slightly increases with increasing external magnetic field (Figure S3b).

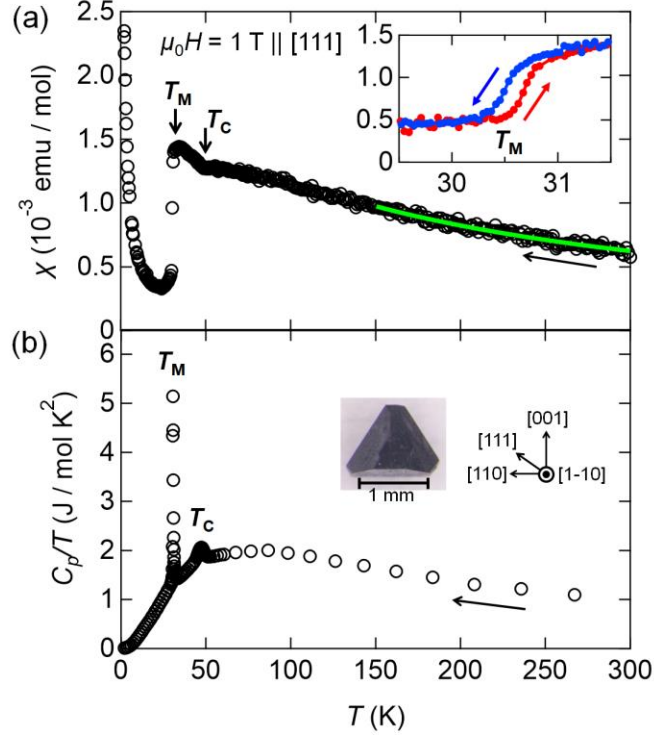


Figure 2. (a) Temperature dependence of the magnetic susceptibility χ for $H \parallel [111]$ of GaNb_4Se_8 . The yellow-green line indicates the Curie-Weiss fit above 150 K. The inset shows an enlarged view of the behavior around T_M . Blue and red circles indicate the data in the cooling and heating processes, respectively. (b) Temperature dependence of the heat capacity divided by temperature, C_p/T , at 0 T. The inset shows a single crystal used for the magnetic susceptibility and heat capacity measurements.

Figure 3a shows the temperature dependence of thermal expansion $\Delta L/L_{300\text{K}}$ along the $[111]$ axis of GaNb_4Se_8 . While a clear increase of about 0.0002% in $\Delta L/L_{300\text{K}}$ is

observed at T_M , no anomaly is observed around T_C with a change of less than 0.0001%. Figure 3b shows the temperature dependence of the integrated intensity of a Bragg peak $-5\ 2\ 0$, which appears below T_C . The appearance of the Bragg reflection of $-5\ 2\ 0$ is attributable to the change from the F to the P lattice. Figures 3c and 3d show the XRD data on the $HK0$ plane at 70 and 40 K, respectively. Although new Bragg peaks appear at reciprocal lattice points with an odd h or odd k , no peak splitting is observed for Bragg reflections in the intermediate-temperature phase. The systematic absence of Bragg peaks at $h00$: $h = 2n+1$ and at $0k0$: $k = 2n+1$ (red triangles in Figure 3d) shows 2_1 screw axes along the principal axes in the intermediate-temperature phase.

Figure 4a shows the crystal structure of GaNb_4Se_8 at 40 K in the intermediate-temperature phase. The space group is $P2_13$, which is consistent with the former powder XRD experiment.²⁰ Details of the structural parameters are summarized in Tables S3 and S4. There are two distinct Nb sites, Nb1 and Nb2, with a ratio of 3:1. There is a difference in the volumes between Se_6 octahedra around Nb1 (gray) and Nb2 (orange), as shown in Figure 4b, which is ascribed to the difference in the valence of the Nb ions. Since the ionic radius of Nb^{3+} and Nb^{4+} are 0.72 and 0.68 Å,⁴⁰ Nb ions coordinated by the larger and smaller octahedra correspond to Nb^{3+} and Nb^{4+} , respectively. In the high-temperature phase, each Nb ion has $7/4$ electrons in the $4d$ orbitals in average. In the intermediate-temperature phase, since Nb^{3+} and Nb^{4+} ions have two and one electrons in the $4d$ orbitals, the total number of $4d$ electrons per Nb_4 cluster is $(2 \times 3) + (1 \times 1) = 7e$.

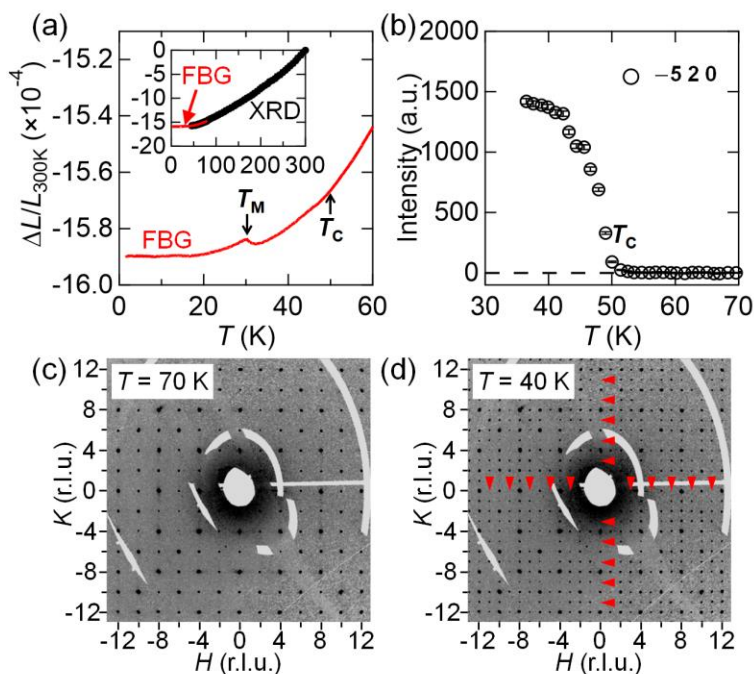


Figure 3. (a) Temperature dependence of thermal expansion $\Delta L/L_{300K}$ along the [111] axis of GaNb_4Se_8 . The inset shows the data up to 300 K. Black dots and red lines indicate the XRD and FBG data, respectively. (b) Temperature dependence of the integrated intensity of the $-5\ 2\ 0$ reflection. (c,d) XRD data on the $HK0$ plane at (c) 70 K in the high-temperature phase and (d) 40 K in the intermediate-temperature phase. Red triangles in (d) indicate positions $h00$: $h = 2n+1$ and $0k0$: $k = 2n+1$, where no Bragg peaks are observed.

Figure 4c shows the molecular orbital scheme, indicating the Nb cluster rearrangement from a tetramer in the high-temperature phase to a trimer-monomer in the intermediate-temperature phase. The Nb-Nb distance in the regular tetrahedron in the high-temperature phase is $3.0345(4)\ \text{\AA}$ (Figure 1a), whereas the Nb1-Nb1 and Nb1-Nb2

distances are 2.9730(4) and 3.1036(4) Å, respectively, in the distorted tetrahedron in the intermediate-temperature phase (Figure 4d). The changes in Nb-Nb distances are approximately 2%, which is significantly larger than the distortion in the overall lattice with a change of less than 0.0001%. In the distorted tetrahedron, three Nb1 atoms form a regular trimer, where two of the three t_{2g} (d_{yz} , d_{zx} , and d_{xy} , shown by red, green, and blue ribbons, respectively, in Figure 4e) orbitals on each Nb1 site form σ bonds. Since a Nb³⁺ ion has two 4d electrons, two electrons are accommodated in each σ -bonding orbital,⁴¹ resulting in the spin-singlet formation. These σ -bonding orbitals correspond to the lower-lying singlet and doublet with three up and three down electrons (Figure 4c). This type of spin-singlet trimer is reported in layered compounds LiVO₂⁴² and LiVS₂.⁴³ A localized $S = 1/2$ spin, represented by an orange arrow in Figure 4c, remains on each Nb2 site in the intermediate-temperature phase. Therefore, each Nb₄ cluster hosts $S = 1/2$ in both the high- and intermediate-temperature phases. However, the unpaired electron is tightly localized on the Nb2 site in the intermediate-temperature phase in contrast to the high-temperature phase. As a result, since the interaction between localized spins in the intermediate-temperature phase is weaker than that in the high-temperature phase, the magnetic susceptibility slightly increases below T_C (Figure 2a). The phase transition at T_C does not involve changes in the cubic lattice or the total magnetic moment. The entropy change of $\Delta S_C = 1.0$ J/(mol K) estimated from the specific heat (Figure 2b) may be mostly attributed to a pure charge component. Considering the degeneracy of the t_2 orbital with $S = 1/2$ in the high-temperature phase (Figure 1c), the released entropy is estimated as $R \ln 3$. The observed $\Delta S_C = 1.0$ J/(mol K) is significantly smaller than $R \ln 3 \cong 9.1$ J/(mol K), suggesting the growth of short-range interactions in the high-temperature phase.

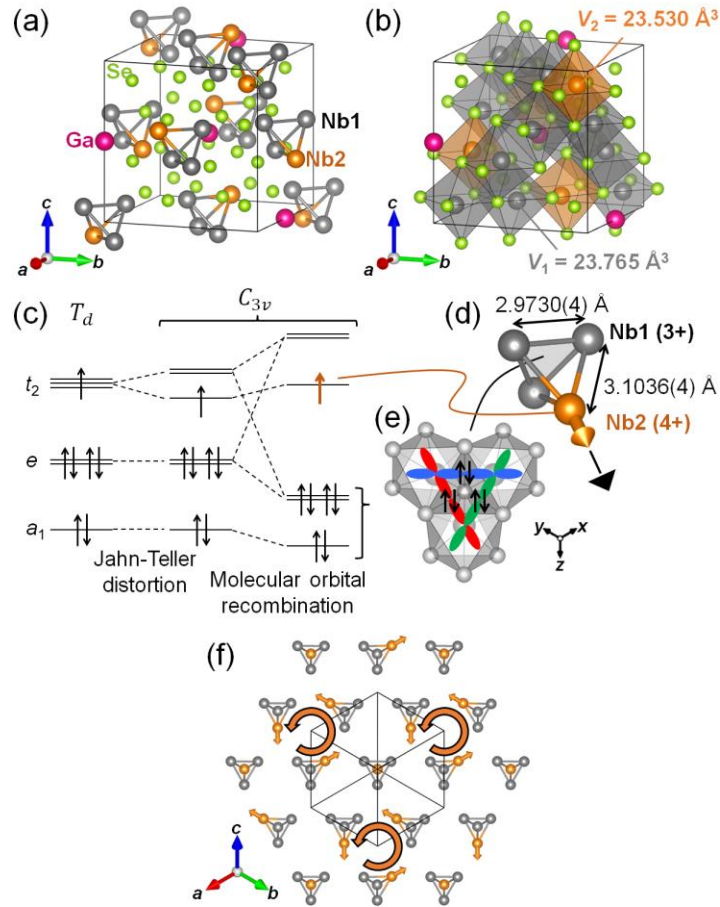


Figure 4. Crystal structure of GaNb_4Se_8 at 40 K in the intermediate-temperature phase, focusing on (a) Nb_4 tetrahedra and (b) NbSe_6 octahedra. (c) Schematic of the molecular orbital recombination indicating the Nb cluster rearrangement from a tetramer to a trimer-monomer. (d) A distorted Nb_4 tetrahedron around $1/2, 0, 1/2$ composed of an Nb1 trimer (gray) and an Nb2 atom (orange). A solid triangle indicates the 3-fold rotation axis, along which a local electric dipole moment is present (an orange vector). (e) Schematic of a spin-singlet formation in a Nb1 trimer. Red, green, and blue ribbons indicate the d_{yz} , d_{zx} , and d_{xy} orbitals extending in the trimer plane, respectively. The x, y, and z vectors indicate the local axes. (f) Vortex arrangement of electric dipole moments at the tetramers on a (111) layer.

A local electric dipole moment on the distorted Nb tetramer is shown by an orange vector in Figure 4d. The electric dipole moments are oriented in four different directions between adjacent tetramers. When viewing one (111) layer, the electric dipole moments form vortices as shown in Figure 4f, corresponding to a chiral charge order. The structural analysis revealed that two enantiomorphic domains exist in equal proportions (Table S4). These two types of domains correspond to the clockwise and counterclockwise vortices of the electric dipole moments. Figure 4f shows the domain corresponding to the counterclockwise vortices. The two domains may show the optical rotation of opposite signs.

A similar elongation of M_4 tetrahedron along one 3-fold rotation axis is observed in GaV_4S_8 ³⁰ and GaV_4Se_8 ,²⁸ where a V ion has 7/4 3d electrons on average. In GaV_4S_8 , all of the tetrahedra are elongated along the same 3-fold rotation axis and the crystal structure changes to polar $R3m$ in the low-temperature phase, where two different V sites form larger and smaller VS_6 octahedra with a ratio of 1:3 (Figure S4).³⁰ If the V site with the larger (smaller) volume of the octahedron is assigned to the V^{3+} (V^{4+}) ion with two (one) 3d electrons, considering the ionic radius,⁴⁰ the total number of 3d electrons per V_4 cluster becomes 5e, which differs from the intermediate-temperature phase of GaNb_4Se_8 with 7e per Nb_4 cluster. Therefore, the low-temperature phase in GaV_4S_8 is not explained by the charge ordering picture but by the simple cooperative Jahn-Teller distortion of the V_4 molecular orbitals. In the case of the simple Jahn-Teller scenario, the strain interaction between adjacent M_4 clusters is ferroic, resulting in the rhombohedral distortion along the $\langle 111 \rangle$ axes like GaV_4S_8 ³⁰ and GaV_4Se_8 .²⁸ On the other hand, in the case of the charge

ordering, the Coulomb interaction favors the antiferroic arrangement between adjacent M_4 clusters like CsW_2O_6 .¹³ The structure realized by this antiferroic arrangement corresponds to the chiral charge order with the cubic symmetry. In the dipole-dipole approximation, it should be noted that the Coulomb energy among the distorted tetrahedra is lower for the cubic (antiferroic) case than for the rhombohedral (ferroic) case (Figure S5 in Supporting Information). Considering that the $4d$ orbitals of Nb are more spatially spread than the $3d$ orbitals of V, the orbital overlap between the M sites and the energy gain attributed to the trimer formation (Figure 4c) are larger in $M = \text{Nb}$ than in $M = \text{V}$. As a result, the CO phase distinct from the rhombohedral distortion is realized only in $M = \text{Nb}$. The activation energies are reported to be 124, 165, and 49 meV in the high-, intermediate-, and low-temperature phases of GaNb_4Se_8 from the electric resistivity.³⁹ The highest activation energy in the intermediate-temperature phase also supports the charge ordering model.

In the case of CsW_2O_6 , each $\text{W}^{5.33+}$ trimer forms a three-centered-two-electron state and the rest of W ions behave as W^{6+} with empty $5d$ orbitals below the metal-insular transition temperature, resulting in a nonmagnetic insulating state.¹³ Therefore, the trimer formation and the nonmagnetic state simultaneously emerge. In GaNb_4Se_8 , a nonmagnetic phase appears below $T_M = 31$ K, which is lower than the charge ordering temperature $T_C = 50$ K. The low-temperature nonmagnetic state of GaNb_4Se_8 may originate from the rearrangement of charges. One may note that the undistorted paramagnetic phase may change directly into nonmagnetic states in GaNb_4S_8 ³² and GaTa_4Se_8 ²⁰ due to the absence of the charge order phase.

CONCLUSIONS

The crystal structure in the intermediate-temperature phase of GaNb_4Se_8 is investigated by synchrotron XRD using a high-quality single crystal. The Nb cluster rearrangement from tetramer to trimer-monomer is driven by the chiral charge order. The Nb^{3+} trimer is stabilized by σ -bonding six $4d$ electrons, while a localized $S = 1/2$ spin remains on the Nb^{4+} ion. The chiral charge order maintains cubic symmetry, which is not found in other lacunar spinel GaM_4X_8 series.

ASSOCIATED CONTENT

Supporting Information.

The Supporting Information is available free of charge at ACS Publications website. Results of the structural analysis, magnetic susceptibility, and heat capacity (PDF)

Corresponding Author

Shunsuke Kitou - Department of Advanced Materials Science, The University of Tokyo, Kashiwa 277-8561, Japan.; E-mail: kitou@edu.k.u-tokyo.ac.jp

Notes

The authors declare no competing financial interest.

ACKNOWLEDGMENT

We thank H. Ishikawa and Y. Okamoto for fruitful discussions, and A. Ikeda for generously allowing us to use an optical sensing instrument (Hyperion si155, LUNA) for thermal expansion. This work was supported by Grants-in-Aid for Scientific Research (No. JP19H05826, JP22K14010, JP23K13068, and JP23H01120) from JSPS. The

synchrotron radiation experiments were performed at SPring-8 with the approval of the Japan Synchrotron Radiation Research Institute (JASRI) (Proposal No. 2023B1603).

REFERENCES

1. Streltsov, S. V.; Khomskii, D. I. Orbital physics in transition metal compounds: new trends. *Phys.-Usp.* **2017**, 60, 1121.
2. Khomskii, D. I.; Streltsov, S. V. Orbital Effects in Solids: Basics, Recent Progress, and Opportunities. *Chem. Rev.* **2021**, 121, 2992-3030.
3. Andersson G. Studies on Vanadium Oxides. *Acta Chim. Scand.* **1956**, 10, 623.
4. Kawakubo, T. Crystal Distortion and Electric and Magnetic Transition in VO₂. *J. Phys. Soc. Jpn.* **1965**, 20, 516.
5. Longo, J. M.; Kierkegaard, P. A Refinement of Structure of VO₂. *Acta Chem. Scand.* **1970**, 24, 420.
6. Kucharczyk, D.; Niklewski, T. Accurate X-ray Determination of the Lattice Parameters and the Thermal Expansion Coefficients of VO₂ near the Transition Temperature. *J. Appl. Crystallogr.* **1979**, 12, 370.
7. Kitou, S; Nakano, A; Imaizumi, M.; Nakamura, Y.; Terasaki, I.; Arima, T. Molecular orbital formation and metastable short-range ordered structure in VO₂. *Phys. Rev. B* **2023**, 109, L100101.
8. Jung, Y.; Jeong, J.; Qu, Z.; Cui, B.; Khanda, A.; Parkin, S. S. P.; Poon, J. K. S. Observation of Optically Addressable Nonvolatile Memory in VO₂ at Room Temperature. *Adv. Electron. Mater.* **2021**, 7, 2001142.
9. Jung, Y.; Han, H.; Sharma, A.; Jeong, J.; Parkin, S. S. P.; Poon, J. K. S. Integrated Hybrid VO₂-Silicon Optical Memory. *ACS Photonics* **2022**, 9, 217-223.

10. Kim, B.-J.; Lee, Y. W.; Chae, B.-G.; Yun, S. J.; Oh, S.-Y.; Kim, H.-T.; Lim, Y.-S. Temperature dependence of the first-order metal-insulator transition in VO₂ and programmable critical temperature sensor. *Appl. Phys. Lett.* **2007**, 90, 023515.
11. Strelcov, E.; Lilach, Y.; Kolmakov, A. Gas Sensor Based on Metal–Insulator Transition in VO₂ Nanowire Thermistor. *Nano Lett.* **2009**, 9, 2322-2326.
12. Hirai, D.; Bremholm, M.; Allred, J. M.; Krizan, J.; Schoop, L. M.; Huang, Q.; Tao, J.; Cava, R. J. Spontaneous Formation of Zigzag Chains at the Metal-Insulator Transition in the β -Pyrochlore CsW₂O₆. *Phys. Rev. Lett.* **2013**, 110, 166402.
13. Okamoto, Y.; Amano, H.; Katayama, N.; Sawa, H.; Niki, K.; Mitoka, R.; Harima, H.; Hasegawa, T.; Ogita, N.; Tanaka, Y.; Takigawa, M.; Yokoyama, Y.; Takehana, K.; Imanaka, Y.; Nakamura, Y.; Kishida, H.; Takenaka, K. Regular-triangle trimer and charge order preserving the Anderson condition in the pyrochlore structure of CsW₂O₆. *Nat. Commun.* **2020**, 11, 3144.
14. Abd-Elmeguid, M. M.; Ni, B.; Khomskii, D. I.; Pocha, R.; Johrendt, D.; Wang, X.; Syassen, K. Transition from Mott Insulator to Superconductor in GaNb₄Se₈ and GaTa₄Se₈ under High Pressure. *Phys. Rev. Lett.* **2004**, 93, 126403.
15. Pocha, R.; Johrendt, D.; Ni, B.; Abd-Elmeguid, M. M. Crystal Structures, Electronic Properties, and Pressure-Induced Superconductivity of the Tetrahedral Cluster Compounds GaNb₄S₈, GaNb₄Se₈, and GaTa₄Se₈. *J. Am. Chem. Soc.* **2005**, 127, 8732-8740.
16. Park, M. J.; Sim, G.; Jeong, M. Y.; Mishra, A.; Han, M. J.; Lee, S. Pressure-induced topological superconductivity in the spin–orbit Mott insulator GaTa₄Se₈. *npj Quantum Mater.* **2020**, 5, 41.

17. Deng, H.; Zhang, J.; Jeong, M. Y.; Wang, D.; Hu, Q.; Zhang, S.; Sereika, R.; Nakagawa, T.; Chen, B.; Yin, X.; Xiao, H.; Hong, X.; Ren, J.; Han, M. J.; Chang, J.; Weng, H.; Ding, Y.; Lin, H.-Q.; Mao, H.-k. Metallization of Quantum Material GaTa₄Se₈ at High Pressure. *J. Phys. Chem. Lett.* **2021**, *12*, 5601-5607.
18. Janod, E.; Dorolti, E.; Corraze, B.; Guiot, V.; Salmon, S.; Pop, V.; Christien, F.; Cario, L.; Negative Colossal Magnetoresistance Driven by Carrier Type in the Ferromagnetic Mott Insulator GaV₄S₈. *Chem. Mater.* **2015**, *27*, 4398-4404.
19. Waki, T.; Kajinami, Y.; Tabata, Y.; Nakamura, H.; Yoshida, M.; Takigawa, M.; Watanabe, I. Spin-singlet state formation in the cluster Mott insulator GaNb₄S₈ studied by μ SR and NMR spectroscopy. *Phys. Rev. B* **2010**, *81*, 020401(R).
20. Ishikawa, H.; Yajima, T.; Matsuo, A.; Ihara, Y.; Kindo, K. Nonmagnetic Ground States and a Possible Quadrupolar Phase in 4d and 5d Lacunar Spinel Selenides GaM₄Se₈ (M = Nb, Ta). *Phys. Rev. Lett.* **2020**, *124*, 227202.
21. Kim, H.-S.; Im, J.; Han, M. J.; Jin, H. Spin-orbital entangled molecular j_{eff} states in lacunar spinel compounds. *Nat. Commun.* **2014**, *5*, 3988.
22. Jeong, M. Y.; Chang, S. H.; Kim, B. H.; Sim, J.-H.; Said, A.; Casa, D.; Gog, T.; Janod, E.; Cario, L.; Yunoki, S.; Han, M. J.; Kim, J. Direct experimental observation of the molecular $J_{\text{eff}} = 3/2$ ground state in the lacunar spinel GaTa₄Se₈. *Nat. Commun.* **2017**, *8*, 782.
23. Petersen, T.; Prodan, L.; Tsurkan, V.; Krug von Nidda, H.-A.; Kézsmárki, I.; Rößler, U. K.; Hozoi, L. How Correlations and Spin–Orbit Coupling Work within Extended Orbitals of Transition-Metal Tetrahedra of 4d/5d Lacunar Spinels. *J. Phys. Chem. Lett.* **2022**, *13*, 1681-1686.

24. Petersen, T.; Bhattacharyya, P.; Rößler, U. K.; Hozoi, L. Resonating holes vs molecular spin-orbit coupled states in group-5 lacunar spinels. *Nat. Commun.* **2023**, *14*, 5218.
25. Yang, T.-H.; Kawamoto, S.; Higo, T.; Wang, S. G.; Stone, M. B.; Neuefeind, J.; Ruff, J. P. C.; Abeykoon, A. M. M.; Chen, Y.-S.; Nakatsuji, S.; Plumb, K. W. Bond ordering and molecular spin-orbital fluctuations in the cluster Mott insulator GaTa₄Se₈. *Phys. Rev. Research* **2022**, *4*, 033123.
26. Kézsmárki, I.; Bordács, S.; Milde, P.; Neuber, E.; Eng, L. M.; White, J. S.; Rønnow, H. M.; Dewhurst, C. D.; Mochizuki, M.; Yanai, K.; Nakamura, H.; Ehlers, D.; Tsurkan, V.; Loidl, A. Néel-type skyrmion lattice with confined orientation in the polar magnetic semiconductor GaV₄S₈. *Nat. Mater.* **2015**, *14*, 1116-1122.
27. Ruff, E.; Widmann, S.; Lunkenheimer, P.; Tsurkan, V.; Bordács, S.; Kézsmárki, I.; Loidl, A. Multiferroicity and skyrmions carrying electric polarization in GaV₄S₈. *Sci. Adv.* **2015**, *1*, e1500916.
28. Fujima, Y.; Abe, N.; Tokunaga, Y.; Arima, T. Thermodynamically stable skyrmion lattice at low temperatures in a bulk crystal of lacunar spinel GaV₄Se₈. *Phys. Rev. B* **2017**, *95*, 180410(R).
29. Schueller, E. C.; Kitchaev, D. A.; Zuo, J. L.; Bocarsly, J. D.; Cooley, J. A.; Van der Ven, A.; Wilson, S. D.; Seshadri, R. Structural evolution and skyrmionic phase diagram of the lacunar spinel GaMo₄Se₈. *Phys. Rev. Materials* **2020**, *4*, 064402.
30. Pocha, R.; Johrendt, D.; Pöttgen, R. Electronic and Structural Instabilities in GaV₄S₈ and GaMo₄S₈. *Chem. Mater.* **2000**, *12*, 2882-2887.
31. Routledge, K.; Vir, P.; Cook, N.; Murgatroyd, P. A. E.; Ahmed, S. J.; Savvin, S. N.;

- Claridge, J. B.; Alaria, J. Mode Crystallography Analysis through the Structural Phase Transition and Magnetic Critical Behavior of the Lacunar Spinel GaMo_4Se_8 . *Chem. Mater.* **2021**, 33, 5718-5729.
32. Geirhos, K.; Langmann, J.; Prodan, L.; Tsirlin, A. A.; Missiul, A.; Eickerling, G.; Jesche, A.; Tsurkan, V.; Lunkenheimer, P.; Scherer, W.; Kézsmárki, I. Cooperative Cluster Jahn-Teller Effect as a Possible Route to Antiferroelectricity. *Phys. Rev. Lett.* **2021**, 126, 187601.
33. Daou, R.; Weickert, F.; Nicklas, M.; Steglich, F.; Haase, A.; Doerr, M. High resolution magnetostriction measurements in pulsed magnetic fields using fiber Bragg gratings. *Rev. Sci. Instrum.* **2010**, 81, 033909.
34. Sugimoto, K.; Ohsumi, H.; Aoyagi, S.; Nishibori, E.; Moriyoshi, C.; Kuroiwa, Y.; Sawa, H.; Takata, M. Extremely High Resolution Single Crystal Diffractometry for Orbital Resolution using High Energy Synchrotron Radiation at SPring-8. *AIP Conf. Proc.* **2010**, 1234, 887-890.
35. CrysAlisPro (Agilent Technologies Ltd, Yarnton, 2014).
36. Petříček, V.; Dušek, M.; Palatinus, L. Discontinuous modulation functions and their application for analysis of modulated structures with the computing system JANA2006. *Z. Kristallogr. Cryst. Mater.* **2014**, 229, 345-352.
37. Momma, K.; Izumi, F. VESTA 3 for three-dimensional visualization of crystal, volumetric and morphology data. *J. Appl. Crystallogr.* **2011**, 44, 1272-1276.
38. Kim, H.-S.; Haule, K.; Vanderbilt, D. Molecular Mott state in the deficient spinel GaV_4S_8 . *Phys. Rev. B* **2020**, 102, 081105(R).
39. Winkler, M.; Prodan, L.; Tsurkan, V.; Lunkenheimer, P.; Kézsmárki, I. Antipolar

- transitions in GaNb_4Se_8 and GaTa_4Se_8 . *Phys. Rev. B* **2022**, 106, 115146.
40. Shannon, R. D. Revised effective ionic radii and systematic studies of interatomic distances in halides and chalcogenides. *Acta Crystallogr.* **1976**, 32, 751-767.
41. Pen, H. F.; van den Brink, J.; Khomskii, D. I.; Sawatzky, G. A. Orbital Ordering in a Two-Dimensional Triangular Lattice. *Phys. Rev. Lett.* **1997**, 78, 1323.
42. Goodenough, J. B.; Dutta, G.; Manthiram, A. Lattice instabilities near the critical V-V separation for localized versus itinerant electrons in $\text{LiV}_{1-y}\text{M}_y\text{O}_2$ (M = Cr or Ti) $\text{Li}_{1-x}\text{VO}_2$. *Phys. Rev. B* **1991**, 43, 10170.
43. Katayama, N.; Uchida, M.; Hashizume, D.; Niitaka, S.; Matsuno, J.; Matsumura, D.; Nishihata, Y.; Mizuki, J.; Takeshita, N.; Gauzzi, A.; Nohara, M.; Takagi, H. Anomalous Metallic State in the Vicinity of Metal to Valence-Bond Solid Insulator Transition in LiVS_2 . *Phys. Rev. Lett.* **2009**, 103, 146405.

Supporting Information of
Cluster rearrangement by chiral charge order in lacunar spinel
GaNb₄Se₈

Shunsuke Kitou¹, Masaki Gen², Yuiga Nakamura³, Yusuke Tokunaga¹, Taka-hisa Arima^{1,2}

¹*Department of Advanced Materials Science, The University of Tokyo, Kashiwa 277-8561, Japan.*

²*RIKEN Center for Emergent Matter Science, Wako 351-0198, Japan.*

³*Japan Synchrotron Radiation Research Institute (JASRI), SPring-8; Hyogo 679-5198, Japan.*

Table S1. Structural parameters of GaNb₄Se₈ at 70 K. The space group is $F\bar{4}3m$ (No. 216) and $a = 10.4143(11)$ Å. Note that $U_{11} = U_{22} = U_{33}$ and $U_{12} = U_{13} = U_{23}$.

Atom	Wyckoff position	Site symmetry	x	y	z	U_{11} (Å ²)	U_{12} (Å ²)
Ga	4a	$\bar{4}3m$	0	0	0	0.003035(13)	0
Nb	16e	.3m	0.396982(4)	= x	= x	0.004115(8)	-0.000372(6)
Se1	16e	.3m	0.635612(5)	= x	= x	0.004135(9)	0.000178(8)
Se2	16e	.3m	0.134355(4)	= x	= x	0.003183(8)	-0.000248(7)

Table S2. Summary of crystallographic data of GaNb₄Se₈ at 70 K.

Wavelength (Å)	0.30956
Crystal dimension (μm ³)	52 × 48 × 35
Space group	$F\bar{4}3m$
a (Å)	10.4143(11)
Z	4
F(000)	1868
(sinθ/λ) _{max} (Å ⁻¹)	1.79
N_{total}	44710
N_{unique}	2629
Average redundancy	17.006
Completeness (%)	100
Number of unique reflections ($I > 3\sigma$ / all)	2575 / 2629
Assuming Ga occupancy = 1 ($N_{\text{parameters}} = 12$)	
R_1 ($I > 3\sigma$ / all)	2.14% / 2.17%
wR_2 ($I > 3\sigma$ / all)	2.46% / 2.47%
GOF ($I > 3\sigma$ / all)	1.76 / 1.74
Flack parameters ($a, b, c: -a, -b, -c$ ($\bar{1}$))	0.994(12) : 0.006(12)
CCDC	2323621
Allowing Ga deficiency ($N_{\text{parameters}} = 13$)	
Occupancy of Ga	0.994(3)
R_1 ($I > 3\sigma$ / all)	2.14% / 2.17%
wR_2 ($I > 3\sigma$ / all)	2.46% / 2.47%
GOF ($I > 3\sigma$ / all)	1.75 / 1.74

Table S3. Structural parameters of GaNb₄Se₈ at 40 K. The space group is $P2_13$ (No. 198) and $a = 10.4138(11)$ Å.

Atom	Wyckoff position	Site symmetry	x	y	z
Ga	4a	.3.	0.498942(6)	= x	= x
Nb1	12b	1	0.598205(4)	0.895622(3)	0.602942(4)
Nb2	4a	.3.	0.893013(5)	= x	= x
Se1	12b	1	0.635199(5)	0.368042(5)	0.362978(5)
Se2	12b	1	0.634497(5)	0.868026(5)	0.363490(5)
Se3	4a	.3.	0.633245(5)	= x	= x
Se4	4a	.3.	0.139546(6)	= x	= x

Atom	U_{11} (Å ²)	U_{22} (Å ²)	U_{33} (Å ²)	U_{12} (Å ²)	U_{13} (Å ²)	U_{23} (Å ²)
Ga	0.002251(8)	= U_{11}	= U_{11}	-0.000016(8)	= U_{12}	= U_{12}
Nb1	0.002112(9)	0.002401(10)	0.002292(11)	0.000014(6)	-0.000032(8)	-0.000403(9)
Nb2	0.002686(8)	= U_{11}	= U_{11}	-0.000148(7)	= U_{12}	= U_{12}
Se1	0.002149(12)	0.002187(10)	0.002192(13)	0.000077(8)	0.000145(8)	-0.000133(9)
Se2	0.002640(14)	0.002726(12)	0.002549(12)	-0.000074(10)	0.000325(9)	0.000021(9)
Se3	0.002193(9)	= U_{11}	= U_{11}	-0.000123(9)	= U_{12}	= U_{12}
Se4	0.002430(9)	= U_{11}	= U_{11}	0.000004(9)	= U_{12}	= U_{12}

Table S4. Summary of crystallographic data of GaNb₄Se₈ at 40 K.

Wavelength (Å)	0.30956
Crystal dimension (μm ³)	52 × 48 × 35
Space group	<i>P2₁3</i>
<i>a</i> (Å)	10.4138(11)
<i>Z</i>	4
<i>F</i> (000)	1868
(sinθ/λ) _{max} (Å ⁻¹)	1.79
<i>N</i> _{total}	178930
<i>N</i> _{unique}	17764
Average redundancy	17.006
Completeness (%)	99.56
<i>N</i> _{parameters}	43
Number of unique reflections (<i>I</i> >3σ / all)	17159 / 17764
<i>R</i> ₁ (<i>I</i> >3σ / all)	2.24% / 2.34%
<i>wR</i> ₂ (<i>I</i> >3σ / all)	2.67% / 2.69%
GOF (<i>I</i> >3σ / all)	1.23 / 1.22
Flack parameters	0.490(15) : 0.008(8)
(<i>a, b, c</i> : - <i>a, -b, -c</i> (1̄): - <i>b, -a, c</i> (.. <i>m</i>): <i>b, a, -c</i> (..2))	: 0.499(8) : 0.003(8)
CCDC	2323622

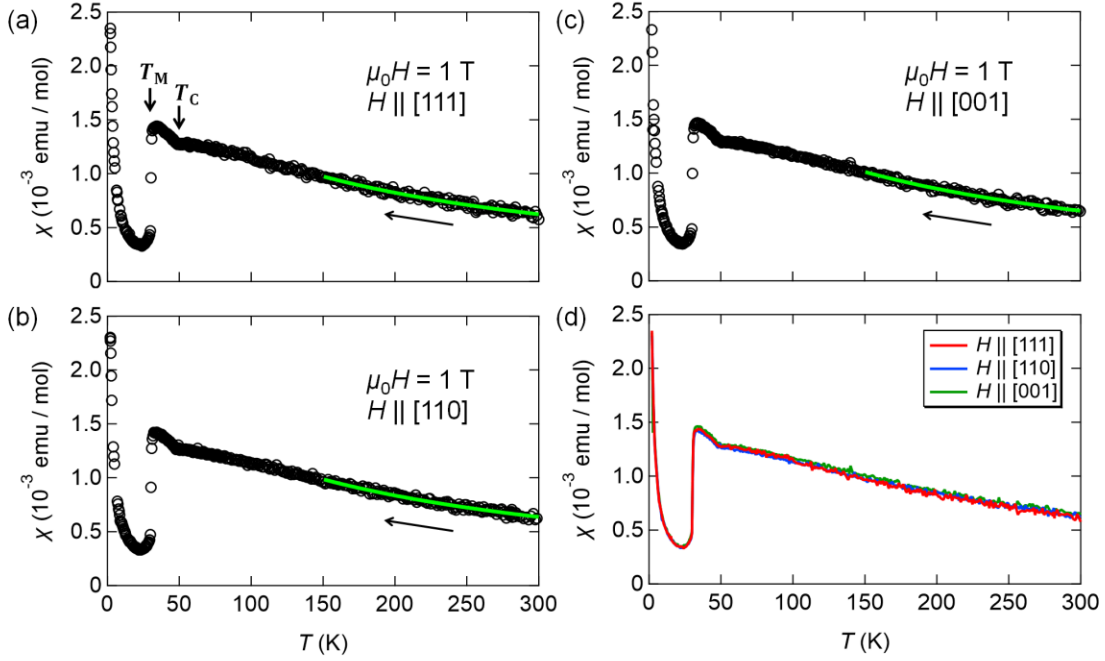


Figure S1. Temperature dependence of the magnetic susceptibility χ for (a) $H \parallel [111]$, (b) $H \parallel [110]$, and (c) $H \parallel [001]$ of GaNb_4Se_8 . Yellow-green lines indicate the results of Curie-Weiss fits above 150 K. (d) The three sets of data (a)-(c) are displayed overlapping.

Table S5. Summary of Curie-Weiss fits for the magnetic susceptibility using a formula $\chi(T) = \chi_0 + C/(T - \Theta)$, where χ_0 , C , and Θ indicate temperature independent terms of χ , Curie constant, and Weiss temperature.

	χ_0 [emu/mol]	C [K emu/mol]	Θ [K]	μ_{eff} [$\mu_B/\text{f. u.}$]
$H \parallel [111]$	-6.2×10^{-5}	0.3033	-142.6	1.558
$H \parallel [110]$	-4.6×10^{-5}	0.3024	-143.1	1.555
$H \parallel [001]$	-4.7×10^{-5}	0.3063	-139.2	1.565

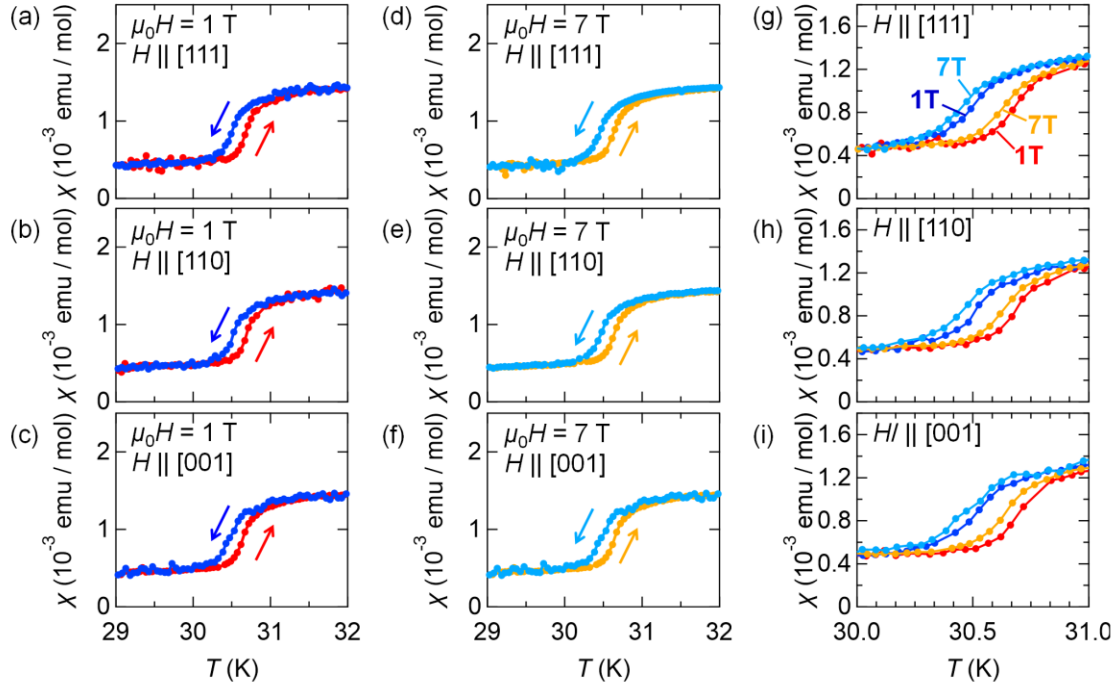


Figure S2. Enlarged views of temperature dependence of the magnetic susceptibility χ for (a) $H \parallel [111]$, (b) $H \parallel [110]$, and (c) $H \parallel [001]$ under the application of $\mu_0 H = 1$ T, and for (d) $H \parallel [111]$ (e) $H \parallel [110]$, and (f) $H \parallel [001]$ under the application of $\mu_0 H = 7$ T. (g)-(i) The data for different external magnetic fields are displayed overlapping. The entropy change at T_M is estimated from the temperature dependence and the external magnetic field dependence of the magnetic susceptibilities using the Clausius-Clapeyron equation $\Delta S_M = -\Delta M \cdot dB/dT_M$. ΔM is calculated using the average difference in the magnetization before and after the magnetic phase transition at $\mu_0 H = 1$ T and 7 T. Since $\Delta M = 0.034$ J/mol T and $dB/dT_M = 6$ T/ -0.03 K are estimated from χ for $H \parallel [111]$ under $\mu_0 H = 1$ T and 7 T, the magnetic entropy change is calculated as $\Delta S_M = 6.8$ J/mol K, which is comparable to the total magnetic entropy $R \ln 2 \cong 5.76$ J/mol K expected for $S_{\text{eff}} = 1/2$.

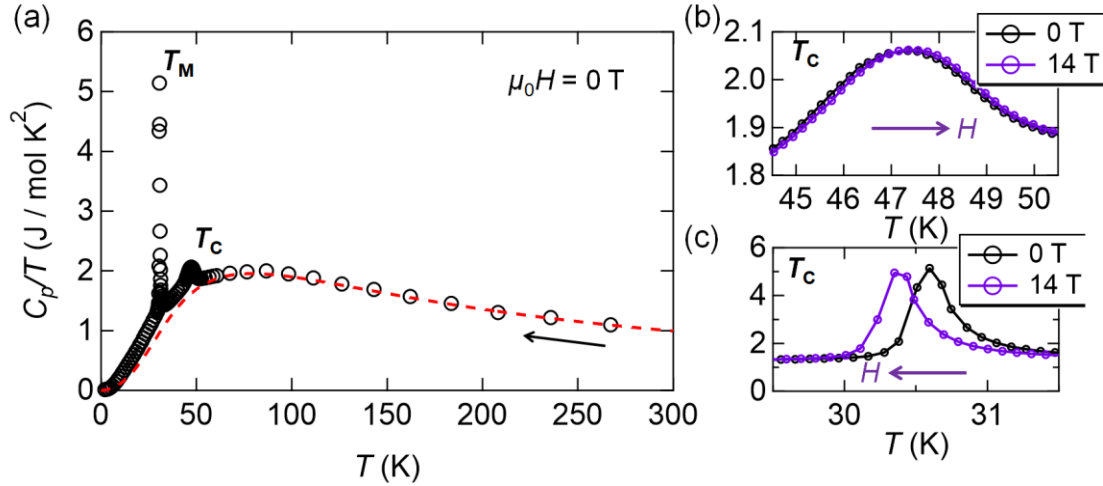


Figure S3. (a) Temperature dependence of the heat capacity divided by temperature C_p/T at 0 T. The data were obtained in a cooling run. The red dashed line denotes the estimated lattice heat capacity C_{fit} based on a two-phonon Debye model. Here, the fitting functions are defined as $C_{\text{fit}} = \frac{1}{3}C_{D_1} + \frac{2}{3}C_{D_2}$, and $C_{D_i} = 9Nk_B \left(\frac{T}{\Theta_{D_i}}\right)^3 \int_0^{\Theta_{D_i}/T} \frac{x^4 e^x}{(e^x - 1)^2} dx$, where $N = 13$ is the number of atoms in the formula unit. The obtained fitting parameters are $\Theta_{D_1} = 600$ K and $\Theta_{D_2} = 250$ K. As mentioned in the main manuscript, the Debye model fails to reproduce the experimental data because a T -bilinear component appears at low temperatures. (b,c) Enlarged views around (b) T_C and (c) T_M . Black and purple dots indicate C_p/T for $H = 0$ and for $\mu_0 H = 14$ T along [111], respectively. T_M decreases with increasing the external magnetic fields, while T_C slightly increases.

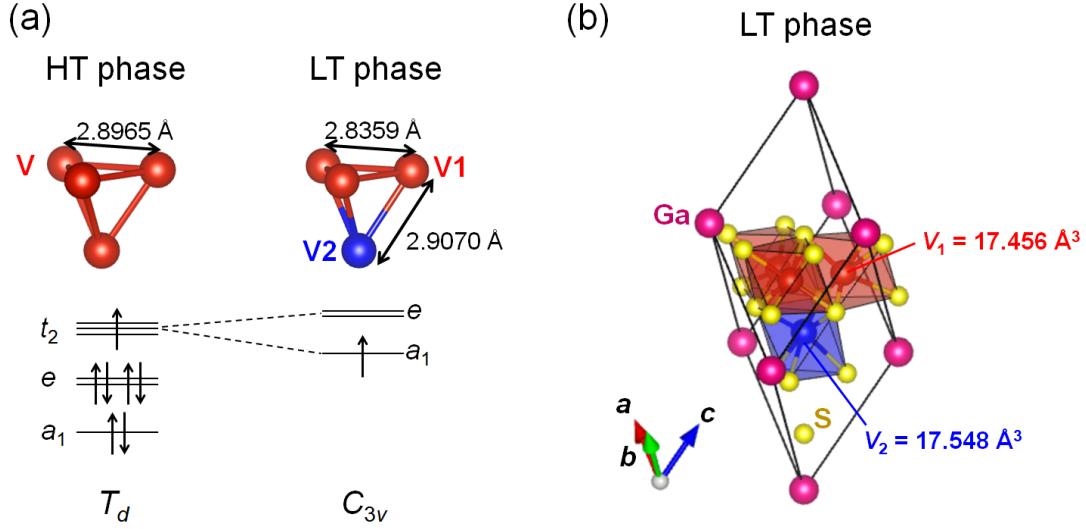


Figure S4. Schematic of a cooperative Jahn-Teller distortion of the t_2 molecular orbitals and crystal structure of GaV_4S_8 at 20 K in the low-temperature phase, referred from [1]. The volumes of V1S_6 and V2S_6 octahedra are 17.456 and 17.548 \AA^3 , respectively, which contradicts the model of V^{3+} trimer- V^{4+} monomer formation.

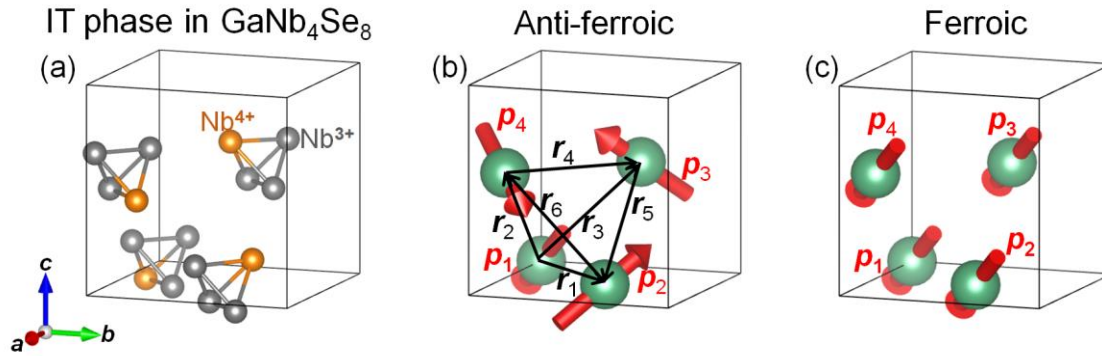


Figure S5. The estimation of Coulomb interactions using the dipole-dipole approximation. (a) The arrangement of the distorted Nb tetramer in the intermediate-temperature (IT) phase of GaNb_4Se_8 . (b) The anti-ferroic arrangement of electric dipole moments (red vectors) corresponding to the IT phase with cubic symmetry. (c) The ferroic arrangement of electric dipole moments with rhombohedral symmetry, similar to GaV_4S_8 [1]. The dipole-dipole interaction is represented by $V_{ij} = \frac{1}{4\pi\epsilon_0 r^3} \left[\mathbf{p}_i \cdot \mathbf{p}_j - \frac{3(\mathbf{p}_i \cdot \mathbf{r})(\mathbf{p}_j \cdot \mathbf{r})}{r^2} \right]$. Here, \mathbf{p}_i and \mathbf{p}_j are the electric dipole moments, and \mathbf{r} is the vector connecting two electric dipoles. In the case of the anti-ferroic arrangement, the Coulomb interaction between each dipole in the four tetramers is $V = \frac{1}{4\pi\epsilon_0 r^3} \left(-\frac{p^2}{3} \right)$. In the case of the ferroic arrangement, the averaged Coulomb interaction between each dipole in the four tetramers is $V = 0$. Therefore, the Coulomb energy among the distorted tetrahedra is lower in the anti-ferroic arrangement than in the ferroic arrangement, resulting in the emergence of chiral charge order in GaNb_4Se_8 .

References

1. Pocha, R.; Johrendt, D.; Pöttgen, R. Electronic and Structural Instabilities in GaV_4S_8 and GaMo_4S_8 . *Chem. Mater.* **2000**, 12, 2882.